

Widespread natural methane and oil leakage from sub-marine Arctic reservoirs

Pavel Serov (✉ pavel.russerov@uit.no)

Centre for Arctic Gas Hydrate, Environment and Climate

Rune Mattingsdal

Norwegian Petroleum Directorate

Monica Winsborrow

The Arctic University of Norway

Henry Patton

Centre for Arctic Gas Hydrate, Environment and Climate <https://orcid.org/0000-0001-9670-611X>

Karin Andreassen

Centre for Gas Hydrate, Environment and Climate

Article

Keywords:

Posted Date: January 13th, 2022

DOI: <https://doi.org/10.21203/rs.3.rs-1225012/v1>

License:   This work is licensed under a Creative Commons Attribution 4.0 International License.

[Read Full License](#)

Version of Record: A version of this preprint was published at Nature Communications on March 30th, 2023. See the published version at <https://doi.org/10.1038/s41467-023-37514-9>.

Abstract

Parceling the anthropogenic and natural (geological) sources of fossil methane in the atmosphere remains problematic due to a lack of distinctive chemical markers for their discrimination. In this light, understanding the distribution and contribution of potential geological methane sources is important. We present empirical observations of hitherto undocumented, widespread and extensive methane and oil release from geological reservoirs to the Arctic Ocean. Methane fluxes from >7,000 seeps significantly deplete in seawater, but nevertheless reach the sea surface and may transfer to the air. Oil slick emission spots and gas ebullition are persistent across multi-year observations and correlate to formerly glaciated geological structures, which have experienced km-scale glacial erosion that has left hydrocarbon reservoirs partially uncapped since the last deglaciation ~15,000 years ago. Such persistent, geologically controlled, natural hydrocarbon release may be characteristic of formerly glaciated hydrocarbon-bearing basins which are common across polar continental shelves, and could represent an underestimated source of natural fossil methane within the global carbon cycle.

Introduction

Release of fluids (liquids and gases) such as methane, from the seafloor is a consequence of diverse chemical, biological, geological and physical processes occurring in the underlying strata, and is pervasive and multifarious across continental margins¹. The magnitude of seafloor methane (CH₄) release reflects the balance between methane generation and its microbial degradation, and between its buoyancy-driven disposition to migrate upwards and the ability of geological layers to retain it. Due to its ability to drive global warming 28 – 36 times more effectively than carbon dioxide over a period of 100 years², natural and anthropogenic methane dynamics in the Earth interiors, oceans and the atmosphere have been a research focus for several decades³. Current rates of increase of atmospheric methane concentration (9.3 ± 2.4 ppb yr⁻¹ during the period 2014 - 2019) are predicted to enhance atmospheric warming over decadal timescales, hindering efforts to stay below the global temperature targets of the Paris Agreement^{4,5}. Yet, a major gap between global methane budgets estimated from inverse modeling (top-down) and from empirical upscaling of point source measurements (bottom-up) demonstrate the incomplete understanding of global methane sources and sinks⁵⁻⁹. Past and present atmospheric methane emissions remain subject to debate largely due to difficulties partitioning contributions of different sources in atmospheric gas records¹⁰. Discriminating the sources of fossil ¹⁴C-free methane (~30% of global methane budget¹¹) such as fugitive emissions during hydrocarbon extraction, coal mining, marine and terrestrial seepage from hydrocarbon basins, etc. is particularly challenging due to often similar $\delta^{13}\text{C}$ and δD composition of the emitted CH₄^{7,8,12}. Because atmospheric data alone do not provide source type information for these isotopically alike emissions, mapping and quantifying the CH₄ inventories and their dynamics is necessary to improve partitioning between anthropogenic and natural sources of fossil methane^{9,13}.

Both top-down and bottom-up approaches to methane budgeting traditionally attribute marine methane sources (including but not limited to submarine clathrates) to microbially mediated degradation of organic matter in shallow sediments (microbial gas)¹⁴⁻¹⁹. *In situ* point source measurements across the ocean floor show that the number of observed microbial methane seeps is greater than thermogenic, which originate from thermal cracking of buried organic matter^{20,21}. Yet data have not been collected systematically and remain scarce, particularly in the Arctic. Owing to this paucity of empirical data, the most recent gridded 1° x 1° methane emission maps reveal only three submarine seep areas in the Arctic, all of which emit predominantly microbial gas²⁰. Two of these are shallow permafrost-bearing shelves off East Siberia and Alaska^{22,23}, whilst the third corresponds to the edge of the gas hydrate stability zone and shallow shelf (80 - 240 m water depth) on the western Svalbard margin^{24,25} (Fig. 1). Seepage of thermogenic CH₄ may lack representation in global emission estimates, in particular when it is considered that 33 million km² of the Arctic shelf area contains hydrocarbon reserves²⁶⁻²⁸ and has experienced successive highly erosive Quaternary glacial cycles²⁹⁻³¹ that are known to promote fluid discharge at the seabed^{32,33} through unsealing of petroleum reservoirs, fault permeability changes^{34,35}, tilting of reservoirs^{36,37}, and pressure-driven expansion of gas and eventual seal failures³⁸. Furthermore, leaking petroleum-bearing basins are prone to concurrent release of both oil and gas, potentially making such settings more efficient for the transportation of CH₄ to the sea surface than just gas seepage sites, as oil coated gas bubbles are thought to be less susceptible to dissolution and, thus, to microbial degradation in the water column^{39,40}.

The Barents Sea shelf represents one such Arctic shelf, with a complex history of uplift and erosion resulting in the removal of 1.7 – 2.6 km of overburden over a period from ~50 Ma BP until the end of the last glacial cycle ~20 ka BP^{41,42}, combined with substantial 2,966 Sm³ mill. o.e. (million standard cubic meters oil equivalent)⁴³ discovered and undiscovered hydrocarbon resources within the Norwegian sector alone.

Here we present seismic data, water column echosounder imaging of gas release, methane concentration measurements in seawater and remote sensing datasets that demonstrate exceptionally extensive hydrocarbon leakage from the subseafloor through the water column and to the sea surface, associated with petroleum systems within the northern Norwegian Barents Sea, Arctic Ocean. These data document for the first time one of the largest cold seep regions in the Arctic, and also evince the first reported natural oil seepage in the Barents Sea. Our empirical data point to a geological setting that is particularly conducive for strong thermogenic hydrocarbon leakage. Hypothesizing such settings may be pervasive across previously glaciated and extensively eroded Arctic continental shelves, we engage two additional less diverse surveys to test whether other geological structures reminiscent to our main study site in Sentralbanken high also emit hydrocarbons (Fig. 1). Observed methane dynamics in the water column across three study sites suggests that naturally uncapped hydrocarbon reservoirs may contribute to methane budgets within ocean water and, possibly, atmosphere and need to be accounted for in Arctic marine methane source estimates.

Geological Settings

The Barents Sea consists of an intricate array of basins hosting a near-continuous sedimentary succession from the Carboniferous to Quaternary, and structural highs bearing fragmented sedimentary succession due to episodes of erosion^{28,31}. The northern Norwegian Barents Sea bears a suite of >10 km wide and 50 – 100 km long anticline structures within the Kong Karls platform and two structural highs – Sentralbanken high and Storbanken high (Fig. 1) all of which were grabens or rift-bounded basins in the Late Paleozoic. Subsequent compression movements initiated in Late Jurassic inverted these basins/grabens²⁸ exhuming older Mesozoic and Paleozoic strata, including Triassic and Jurassic hydrocarbon source and reservoir units^{28,43}.

The hydrocarbon potential of the northern Norwegian Barents Sea is estimated to be significant.⁴³ However, traces of hydrocarbons are frequently found in “dry” wells and surface sediments suggesting hydrocarbon loss due to widespread paleo fluid leakages^{32,50}. Resonating with geochemical observations, basin modeling results³⁴ suggest that the sealing potential of hydrocarbon reservoirs may be compromised due to regional uplift and 850 - 1370 m net erosion in Paleogene and Neogene^{41, 51} and 940 to 1180 net glacial erosion during >40 reciprocal glaciations in Pleistocene⁴².

Across the northern Norwegian Barents Sea, the main source rock with confirmed hydrocarbon potential is the Lower – Middle Triassic Steinkobbe Formation, which consists of organic-rich (2.4 – 10% total organic carbon) marine and delta front fine-grained deposits^{52,53}. This source rock is overlain by at least four potential reservoir units: Kobbe, Snadd, Tubåen and Stø Formations – all deposited during early Mesozoic infilling of the Barents Sea basin with coastal, deltaic and shallow marine terrigenous deposits⁵² (Fig. 2). In contrast to the reservoir formations, deposition of low permeability seal units across the Barents Sea was limited. The most prominent seal is the Upper Jurassic Hekkingen and Fuglen Formations which covers the entire succession of Triassic and Jurassic reservoirs (Fig. 2). Upper Triassic marine shales of the Norian Flatsalen Formation, Lower Ladinian shales and sporadic Upper - Middle Triassic transgressive marine shale beds may also constrain fluid migration.

Results

Oil and gas in sea water

At Sentralbanken high we identified 4,137 acoustic ‘flares’ diagnostic of bubble emission sites (seeps) within a 681 km² area covered with discrete multibeam swaths. Data reveal a strongly heterogenous spatial distribution of the flares, where the majority of the population is grouped in 1 km² to >7 km² distinctive clusters with sharp boundaries (Fig. 3). Solitary flares, which do not have any neighbours within a 500 m radius, comprise only 2.7% of the total flare number. In plan view, the seepage clusters appear as isometric patches unevenly distributed across the structural high with the most pronounced flare clusters gravitating towards its central part. We did not observe any elongated strings of flare

reminiscent of fault lineaments^{54,55} or clusters following certain bathymetric contours as would be expected if the edge of a gas hydrate stability zone defined the gas release^{56,57}. The central part of the Sentralbanken structural high demonstrates the highest gas flare density (Fig. 4a). Here, the flare clusters with clear-cut boundaries show maximum flare densities exceeding 100 seeps per km². These clusters also contain higher ratios of strong and moderate flares (>50% in total) compared to other zones of the Sentralbanken high, where weak flares comprise the considerable majority of flare population (Fig. 4). Across the entire data set, we classified 620 strong flares, 1,384 medium flares, and 2,133 weak flares, defined by their apparent backscatter strength and height reached within the water column (Fig. 3e). Based on the observed spatial distribution of flare clusters and their semi-quantitative characteristics (flare density and proportions of strong, moderate and weak flares), we outline three seepage zones (Fig. 4a). The seepage zones demonstrate a NE orientation, similar to the dominant orientation of the regional structural elements: Sentralbanken high, Storbanken high and elements of Kong Karls platform (Fig. 1).

Outside the most pronounced seepage zones, flare clusters gradually become rarefied and their margins less well defined (Fig. 4c). Within such rarefied, patchy flare clusters, the seep density does not exceed 60 flares * km⁻² and weak flares compose >76% of the total population, consistent with more obstructed advection of fluids through strata or a weaker gas source (Fig. 3, 4).

89 flares, in addition to producing a very strong backscatter signal, also appear to reach close (<50 m) to sea surface before terminating or leaving the echosounder footprint (Fig. 3). Because the height of the insonified water column decreases with increasing swath angle (see Methods), detecting accurate termination of such high flares is only possible within a narrow corridor directly beneath an echosounder, even with 50% swath overlap. This suggests that the actual number of seeps reaching the upper water column section may be substantially larger.

Examining synthetic aperture radar (SAR) images over a 7 month period, we identified persistent oil slicks on the sea surface in Sentralbanken region (Fig. 5a, c). These could be linked to three oil emission sources located at the edge of seepage zone 1 where gas release is somewhat tempered compared to the most intense seepage zones 2 and 3 (Fig. 4). The shape and orientation of the surface slicks varied due to surface current conditions (Fig. 5c). Typically, the slicks formed 7-10 km long and 0.2 -1 km wide stripes and were easily visible on sea surface during the CAGE 21-4 research cruise (Fig. 5b).

In line with abundant acoustic evidence of seafloor gas release, water samples indicate that the entire water column is supersaturated with methane. All collected seawater samples show high (35 to 752 nM) concentrations of dissolved CH₄ in the bottom water layer and in the intermediate water interval (8.5 to 22.8 nM). Notably, all water samples from the surface mixed layer reveal CH₄ concentrations that exceed the sea water – air equilibrium (Fig. 5d) suggesting that CH₄ is diffusing to the air. Given that the seabed seepage is continuously replenishing the seawater CH₄ pool across a ~40 x 70 km area, the cumulative input of this potential CH₄ source deserves attention.

The composition of hydrocarbon gas in sediments reveals a fraction of heavier methane homologs indicative for a thermogenic origin of gas¹. All samples (n=36) collected from four sediment (Fig. 5a) contained 0.3–6.8% ethane, 0–2.5% propane, as well as a suite of less abundant heavier homologs. Core GC 347 collected at the deepest (360 m water depth) zone of the study area from a 5 m tall and 120 m diameter seafloor mound structure revealed gas hydrates. Other cores collected at 301 – 330 m water depth did not contain hydrate, nor did they reveal sediment textures (e.g. moussy sediment) circumstantially evident for recent gas hydrate decomposition.

Geological control of fluid release

Sub-seafloor geology appears to rigidly control the clustering of gas flares. The apex of the Sentralbanken high bears several anticline structures with eroded tops, exposing reservoirs of the Middle Triassic Kobbe Formation and providing 2 - 5 km wide 'windows' for unconstrained fluid discharge (Fig. 6). Each of these 'windows' corresponds to a prominent seepage zone with an extremely high density of seeps (Fig. 3, 4a, 6). Despite the presence of bright spots indicative of fluid accumulations in the sub-seafloor scattered across the entire apex of the Sentralbanken high, strong seabed fluid release is restricted to those parts with subcropping reservoir formation (Fig. 6). The uppermost Kobbe Formation reservoir is connected to deeper reservoirs of Klappmys and Havert Formations by faults and may therefore act as a transitional capacitor for fluids originating from deeper strata, including Upper Paleozoic levels.

On the flanks of the structural high where the overburden remains and the reservoir formation is tapered compared to its apex (Fig. 6), several small flare clusters with a seep density < 50 seeps* km⁻² correlate to the faults piercing down to the top Kobbe Formation. In such settings all seepage correlates to faults.

Within the apex area of the Sentralbanken high where the reservoir formation reaches its maximum thickness and accommodates scattered bright spots, normal faults potentially promoting fluid migration toward the seafloor are abundant. However, there is no consistent correlation between seep intensity and faulting, with the highest seep densities (>100 seeps*km⁻²) not always associated with faults visible on our seismic data (Fig. 6). Furthermore, we observe no apparent correlation between bright spot distribution below the seabed and the location or magnitude of seabed release of gas, with bright spots occurring beneath anomalously strong leakage areas, as well as areas with temperate and no leakage. It is therefore not clear whether faulting plays a significant role in modulating seepage at exhumed and partially subcropping reservoirs that are already preconditioned for strong degassing through erosion. However, on the flanks of the structure where overburden remains, faulting appears to be the dominant mechanism driving tempered seabed gas release. .

A veneer of Quaternary unlithified sediments is not detectable on the conventional seismic profiles (~20 m vertical resolution at the seafloor) available from the study area. However, higher resolution sub-bottom profiler data document a ~3 – 10 m thick layer of glacial deposits (Fig. S1). Furthermore, occasional iceberg ploughmarks, meltwater channels and pockmarks visible on multibeam bathymetry data are

consistent with a drape of unlithified deposits covering the lithified Mesozoic sedimentary strata. However, we do not find correlation between the presence of pockmarks and seabed seepage (Fig. S2).

Methane leakage from other eroded structural highs

To test whether the strong hydrocarbon discharge identified from the eroded structural high setting of Sentralbanken is a circumstantial phenomenon, or whether hydrocarbon leakage may be expected in similar geological settings elsewhere across the formerly glaciated Barents Sea shelf, we investigated the relation between water column gas flares and the structural boundaries of the Storbanken high and anticline structures within the Kong Karls platform, north of Sentralbanken high (Fig. 7). Multibeam echosounder datasets from Kong Karls platform (a discrete line survey), and Storbanken High (an 2,810 km² areal data set acquired by the MAREANO seabed mapping project) both reveal intensive gas flaring confined to emerged structural elements (Fig. 7). At Kong Karls platform, SW and SE anticlines expose the Snadd Formation at the seafloor in their core parts⁴³ (Fig. 2), and correlate closely to 597 gas flares. In Storbanken high, 2,646 flares within an 2,810 km² area are identified, and the most distinct flare strings correlate to subcropping upper Triassic Snadd Formation and lower-middle Jurassic Tubåen and Stø Formations^{43,58} (Fig. 2, 7).

Figure may be

Discussion

Capping effect of overburden

Our datasets from across the Central Barents Sea reveal 7,380 hydrocarbon gas seeps originating from eroded structural highs bearing thermogenic hydrocarbon sources. Aiming to address whether such extensive hydrocarbon gas venting may be significant in the context of global marine methane seepage, we compare our gas flare mapping results with other pronounced marine seep regions that have been surveyed with echosounder systems.

Extensive gas flaring has been documented along the continental margin off Svalbard and along the western margin of the Barents Sea shelf from Bear Island to Kongsfjorden^{24,54,59}. >1,000 gas flares occur within a ~600 x 50 km stretch of this continental margin and fuel a large plume of dissolved methane in the water column⁵⁴. The pronounced Hornsund Fault Zone has been hypothesised to control subseafloor fluid migration, while shrinkage or expansion of the gas hydrate capacitor driven by seasonal water temperature fluctuations^{24,56} may further mediate seabed release. However, the shallowest seep clusters are located at 90 and 240 m water depth and are therefore significantly outside of the gas hydrate stability envelope. The stable isotope composition of emitted methane and absence of heavier methane homologs indicate a microbial gas origin^{54,60,61}.

Along the northern US Atlantic margin, ~570 seeps were identified within 94,000 km² at 50 – 1,700 m water depth, ~440 of which originate at water depths bracketing the upper limit of the gas hydrate stability zone⁵⁷, similar to parts of the western Svalbard margin^{24,56}. The origin and migration pathways of the gas are not clear, yet dynamics of the upper gas hydrate stability zone limit is hypothesized to control seep occurrences⁵⁷.

In contrast to the northern US Atlantic margin and the continental margin west of Svalbard, at Sentralbanken high, the gas seep clusters crosscut bathymetric contours and appear across a wide range of water depths, which is not characteristic for gas release fuelled by the retreat of a gas hydrate layer. However, recovery of gas hydrates at 360 m water depth show that the deepest SW parts of the structural high may be within the zone of gas hydrate stability. We note that seabed gas release is less pronounced at this deeper region, yet it also lies outside of the eroded structural top. At the apex of Sentralbanken high, the absence of a seismic bottom simulating reflector and no confirmed gas hydrate recoveries, together with very extensive and geologically constrained seepage (Fig. 6) suggest that there is no gas hydrate layer capping natural degassing of petroleum reservoir today. At Storbanken high and Kong Karls platform, shallower (~100 – 290 m) water depths point to very limited potential to host pressure and temperature dependent gas hydrates.

In continental margin settings off Western Svalbard and the northern US Atlantic margin, the sedimentary overburden may limit fluid release^{25,57}. However, across the uplifted, eroded and repeatedly glaciated Barents Sea shelf, the sedimentary rock overburden has been significantly reduced⁴², and only a thin veneer of marine and glacial deposits of the last glacial-interglacial cycle overlay the erosional surface of the Mesozoic sedimentary succession. The reduced capping effect of the overburden and limited capping effect of gas hydrates, together with hydrocarbon abundance in the shallow subsurface, provide the ideal geological setting for extensive seepage. Based on the timing of the last Barents Sea ice sheet collapse⁶² – the last major erosional event to affect this region – hydrocarbon leakage associated with the degradation of the overlying overburden seal has been possible, and potentially ongoing, for the last c. 15,000 years, at least.

At the three Barents Sea sites 7,380 seeps have been identified within 3,730 km² of surveyed area (Fig. 7). This density of seepage significantly exceeds the ~1,000 seeps within 30,000 km² of the Western Svalbard margin⁵⁴ and the 570 seeps within 94,000 km² of the northern US Atlantic margin⁵⁷. Given limited water column data coverage (Fig. 7, Fig. S3), we can confidently assume that the actual number of seeps within investigated structures in the northern Norwegian Barents Sea must be substantially higher, making this one of the most active submarine methane release hotspots globally.

Methane dynamics in sea water

Because free methane gas is not subject to microbial degradation in the water, bubble transport through the water column is a potent delivery mechanism to the atmosphere⁴⁰. Methane from marine seep sources has been shown liberating to the atmosphere at shallow shelf settings (20 - 50 m water depth at

Santa Barbara Channel offshore California⁶³, < 50 m water depth on the East Siberian Arctic shelf⁶⁴, 50 – 120 m water depth offshore Svalbard⁶⁵, etc.) where gas bubbles reach close to the sea surface. In deeper water settings, the longer exposure of bubbles to sea water decreases the transport efficacy. However, large, persistent and dense methane seep clusters may be prerequisite for enhanced free gas transportation through the water column due to the creation of a smaller concentration gradient between the methane plume and seawater, which may slow down bubble dissolution^{40,66}. We encountered a water column supersaturated with respect to atmospheric methane equilibrium at all sampling stations, pointing towards the expansion of the methane plume across the actively seeping area. We further detected at least 80 seeps reaching the surface mixed layer and enrolled in sea-air gas exchange (Fig. 4e), and consider it highly likely that there are more beyond our limited multibeam echosounder data coverage in the shallow water column sections. It is interesting to note that the Sentralbanken study site has been circumstantially investigated in terms of methane mixing ratios in air prior to our discovery of seabed gas and oil seepage⁶⁷. Methane mixing ratios above the structural high were found to exceed 2,000 ppb during the autumn and winter months⁶⁷ (the background methane mixing ratio is ~1,950 ppb). Platt et al.⁶⁷ interpreted the excursions from baseline methane mixing ratio as long-distance transport from land-based sources, however, our new findings should motivate re-examination of atmospheric methane concentrations in this area.

The simultaneous release of both methane gas and oil at Sentralbanken high, may contribute to the extreme size and density of free methane gas transport in the water column at this site. Oil coating of methane bubbles is known to increase their lifetime in the water column⁶⁸. The presence of persistent oil slicks within the seepage area and observations of oil droplets reaching the sea surface during sampling of these slicks, indicate that oil is leaking from the seafloor and reaching the sea surface. However, our methane concentration data collected within oil slicks visible both on sea surface and on SAR data, did not show elevated methane content compared to surface water samples collected outside the slicks (Fig. 6), nor was gas ebullition identified during sampling despite smooth sea-surface conditions. Video-guided bubble collection above the seafloor is therefore necessary to confirm if oil coats gas bubbles or gas and oil travel through the water column independently.

Implications for formerly glaciated hydrocarbon-bearing shelves

Our datasets from the Barents Sea document extensive oil and methane leakage from hydrocarbon reservoirs that have experienced uplift and glacial erosion, constituting an important source of methane to the water column, and, possibly, atmospheric inventory. Significantly, there are numerous analogous geological settings (sedimentary basins with petroleum potential that have experienced uplift and glacial erosion) across North Atlantic and Arctic continental margins where we may expect abundant hydrocarbon leakage: the Timan-Pechora Basin in the Pechora Sea³¹, the Sverdrup Basin on the northern margin of North America⁶⁹, the Eastern Basin in the Russian part of the Barents Sea⁴⁵, the western (Norwegian) part of the Barents Sea⁴¹, sedimentary basins surrounding British Isles^{46,70} and sedimentary

basins of western and eastern Greenland^{47,71,72} (Fig. 1). Indeed, landscape evolution modeling^{37,48} suggests that several of these are more severely eroded than the Barents Sea shelf, for example, the eastern and western Greenland shelf, Canadian Arctic Archipelago and Norwegian Sea shelf, increasing the likelihood of reservoir seals being weakened or removed. However, studies of ongoing free gas release across these frontier basins are currently lacking. Expanded mapping and quantifying of seabed point-source emissions across high latitude glaciated shelves should be prioritised and may motivate rethinking of the contribution of thermogenic methane to global marine carbon sources.

Methods

To find relationships between petroleum systems and natural hydrocarbon leakage we combined five sets of multibeam water column data (four CAGE data sets of scattered lines and one aerial MAREANO data set), a suite of 2D seismic lines and existing seismic interpretation results, as well as a series of SAR satellite images and discrete analyses of sea water and bottom sediments (Fig. S3). CAGE data sets were acquired in four research cruises onboard RV Helmer Hanssen: CAGE 18-1 cruise in May 2018, CAGE 19-2 cruise in July 2019, CAGE 20-2 cruise in July 2020 and CAGE 21-4 cruise in August 2021.

Water column backscatter data acquisition

We used multibeam echosounder data to identify gas emission sites from the seafloor to the water column. Multibeam echosounders emit sound waves and measure the elapsed time for a wave to reach a reflective object and return to the receiver (two-way travel time). The distance to the object is calculated based on a sound velocity profile. Because gas bubbles are excellent reflective targets due to their high acoustic impedance contrast with sea water⁷³, surveying water column with multibeam systems is an effective and reliable method for identifying submarine gas discharge sites^{74,75}.

All CAGE data sets were acquired with Kongsberg EM302 echosounder. The EM302 echosounder was operated with a 120° opening angle providing a swath of 432 soundings which covered an off-track area ~3 times the water depth. The ping rate was automatically adjusted depending on the water column thickness. A thicker water column increases the travel time of the acoustic signal and dictates longer intervals between pings. The datasets were acquired at 6-8 knot vessel speed. For sound velocity profile acquisition, we used SBE 911plus CTD sensor.

Publicly available MAREANO data sets were acquired by a third-party using Kongsberg EM710 multibeam system (see <https://www.mareano.no/> for more details on data acquisition).

Water column backscatter data interpretation

Acquired fan-shaped water column images (both, CAGE and MAREANO data sets) have distinctive side-lobe artefacts due to strong signal return from the seafloor within peripheral sectors of the swath (Fig. 3e, f, Fig. S4). The side-lobe artefacts appear outside of a half-circle (minimum slant range) with a radius equal to the shortest distance between the sonar and the seafloor (Fig. S4). The side-lobe artifacts are

inevitable features of the multibeam water column data⁷⁵⁻⁷⁷, which limit the data sector suitable for flare detection to ~50% of the total swath coverage (Fig. 3e, f, Fig. S4). This natural data limitation is broadly known in marine geophysics community⁷⁵⁻⁷⁸.

The transmit fan of the Kongsberg EM302 is split in 4 sectors (Fig. S4) with independent steering to compensate for the vessel movements. Because the sectors have slight ping offsets, small static artefacts appear within the slant range limits (Fig. S4). The artefacts occur at a narrow depth interval from beam 1 to beam 33 and from beam 255 to beam 288 and do not significantly obstruct manual flare detection. MAREANO data acquired with Kongsberg EM710 have very minor static artifacts that do not hinder flare detection.

For gas seep mapping we used only 'observable water volume' where data quality allowed confident acoustic flare detection (Fig. S4). Within the observable volume of multibeam data, acoustic flares appear as clouds of strong scatter points. The position of each point is described by coordinates and water depth. We examined the entire volume of observable water in fan-view mode (Fig. 3f) in FMMidwater software by QPS and manually allocated (picked) coordinates of the visible flare roots. In cases of data overlap, we picked flares during the first passage only.

Comparing acoustic flares with in-situ observations of seabed gas release at the western Svalbard margin, Sahling et al.⁵⁹ showed that strong flares correspond to six clustered streams of bubbles on average, while weak flares typically represent a single bubble stream. Thus, acoustic flares may represent a wide range of gas emission strength and counting them in an indiscriminate way may hinder spatial variability of the gas emissions. With the aim to map the activity of the gas release at detail, we opted for categorizing each acoustic flare within our datasets to weak, medium and strong based on the signal scattering strength (Fig. 3f). Similar subjective assessment of the apparent flare magnitude has been previously done⁷⁹. Aiming to ensure equability of data interpretation, all data were interpreted by one person and with constant colour range indicative for the range of signals and using the same screens. Random inspection of maximum scattering strength within flares has been also done. We assumed that strong flares have raw amplitudes exceeding 65, and weak flares demonstrate raw amplitude below 85. These values have been used for verification of flare strength interpretations throughout the data analysis. Scattering strength may be the best available verification criteria as the dimensions of flares on water column images may depend on the oceanographic conditions (e.g. currents and stratification of water column) and varying beam-footprint width within the swath⁸⁰.

The picked flare locations were plotted as point maps and density maps (Fig. 3, 4). Density maps do not take into account the differences between weak, medium and strong flares and rather show the concentration of individual flares as color-coded polygons. To produce the density maps we utilized interpolation method described by quartic Kernel function (1). Interpolation was done within search radius of 500 m.

$$K(y) = \frac{15}{16}(1 - y^2)^2, |y| \leq 1 \quad (1)$$

Oil slick detection on SAR images

Sentinel-1 Synthetic Aperture Radar (SAR) satellite images were downloaded from the Copernicus Open Access Hub (<https://scihub.copernicus.eu/dhus/#/home>). A selection of seven weather compliant Sentinel-1 images from April to October 2020 was used in this study. Interpretation of oil slick outlines (Fig. 5c) was done manually in ArcGIS based on low backscatter areas with oil slick appearance. The oil slick emission points (Fig. 5a) were determined based on the locations of all interpretations of oil slicks outlines in the three identified areas with large persistent oil slicks.

2D seismic acquisition and processing

CAGE seismic data were acquired using one GI (Generator-Injector) air gun as the seismic energy source. We used a 100-m long streamer with 32 channels separated by 3.125 m, which was composed of four consecutively connected 25 m long P-Cable streamer sections⁸¹. Data processing was done in Radex Pro software and included CDP binning (3.125 x 3.125 m bin size), Simple Bandpass filtering (10-25-300-400 Hz) and Spherical Divergence, bubble removal, NMO correction to water velocity, zero-offset demultiple, migration using the post stack Kirchhoff migration algorithm. Output Seg-y data were interpreted in Petrel Software.

Subbottom profiler (Chirp) data acquisition

The X-STAR Full Spectrum Sonar, transmitting a pulse linearly swept over a spectrum of frequencies (1.5 kHz to 9kHz) and operated at 0.3 Hz ping rate, was used to image the shallow 0 – 30 m of subseafloor in detail. Acquired data did not need manual processing and allowed for distinguishing laminated soft marine sediments, glaciogenic deposits and lithified rocks (Fig. S1).

Measurements of dissolved methane concentration in sea water

Water samples were collected with a CTD rosette and transferred into 120-ml glass bottles immediately after sampling. We added 1 ml of 1M solution of NaOH into each bottle before capping them with a rubber septum and sealing with aluminium crimp caps. Before gas chromatographic analysis with flame ionization detector (GC-FID), 5 mL of laboratory pure N₂ gas was added to the bottles. GC-FID analyses were carried out using ThermoScientific Trace 1310 gas chromatograph.

Measurements of hydrocarbon gas composition in bottom sediments

Sediment samples were collected with a gravity corer. For subtracting a gas phase from a sediment matrix, we used a conventional headspace gas sampling technique. 5 mL of bulk sediments were

transferred into 20-mL glass vials containing 5 mL of 1M solution of NaOH and two glass beads. Vials were capped with a rubber septum and sealed with crimp tops. Analyses were carried out using a ThermoScientific Trace 1310 gas chromatograph equipped with ThermoScientific TG-BOND alumina (Na_2SO_4) 30 m x 0.53 mm x 10 μm column.

Data Availability

Geophysical, geochemical and oceanographic data acquired by CAGE (Fig. 5, S3) will be available upon request to the corresponding author. Seismic data from NPD – Norwegian Petroleum Directorate are available upon direct request. Sentinel -1 SAR images are available at <https://scihub.copernicus.eu/>. MAREANO multibeam echosounder data are available at <https://www.mareano.no/en/maps-and-data/marine-geospatial-data>.

Declarations

Acknowledgement

We thank the crew of RV *Helmer Hanssen* for providing invaluable support for empirical data acquisition; Dr. Andreia Plaza-Faverola for leading CAGE 18-1 research cruise and providing multibeam data; Dr. Malin Johansson for useful discussions of remote sensing data; Frank Werner Jakobsen for providing photographs of oil slicks. The research is supported by the Research Council of Norway through its Centres of Excellence funding scheme (Grant 223259) and by The Norwegian Academy of Science and Letters through its VISTA grant program.

Author contributions

P.S. processed and interpreted multibeam echosounder data, drafted the manuscript and designed the figures. R.M. interpreted satellite SAR images, provided conventional seismic data interpretation; M.W., and H.P., K.A. acquired multibeam echosounder, high-resolution seismic, oceanographic data; K.A., R.M., H.P., M.W., P.S. designed empirical data acquisition campaigns and outlined the scopes of the study. K.A., R.M., H.P., M.W. contributed to manuscript writing and editing.

Competing interests

We declare no competing interests in relation to this research article

References

1. Judd, A. & Hovland, M. *Seabed fluid flow: the impact on geology, biology and the marine environment*. (Cambridge University Press, 2009).
2. Shindell, D. T. *et al.* Improved Attribution of Climate Forcing to Emissions. *Science* **326**, 716–718, doi:10.1126/science.1174760 (2009).
3. Dlugokencky, E. J. (ed NOAA / Global Monitoring Laboratory).
4. Nisbet, E. G. *et al.* Very Strong Atmospheric Methane Growth in the 4 Years 2014–2017: Implications for the Paris Agreement. *Global Biogeochemical Cycles* **33**, 318–342, doi:https://doi.org/10.1029/2018GB006009 (2019).
5. Masson-Delmotte, V. *et al.* (Cambridge University Press Cambridge, UK, 2021).
6. Etiope, G. & Schwietzke, S. Global geological methane emissions: An update of top-down and bottom-up estimates. *Elementa: Science of the Anthropocene* **7**, doi:10.1525/elementa.383 (2019).
7. Kirschke, S. *et al.* Three decades of global methane sources and sinks. *Nature Geoscience* **6**, 813–823, doi:10.1038/ngeo1955 (2013).
8. Saunoy, M. *et al.* The Global Methane Budget 2000–2017. *Earth Syst. Sci. Data* **12**, 1561–1623, doi:10.5194/essd-12-1561-2020 (2020).
9. Thornton, B. F. *et al.* Conflicting estimates of natural geologic methane emissions. *Elementa: Science of the Anthropocene* **9**, doi:10.1525/elementa.2021.00031 (2021).
10. Hmiel, B. *et al.* Preindustrial 14CH₄ indicates greater anthropogenic fossil CH₄ emissions. *Nature* **578**, 409–412, doi:10.1038/s41586-020-1991-8 (2020).
11. Lassey, K. R., Etheridge, D. M., Lowe, D. C., Smith, A. M. & Ferretti, D. F. Centennial evolution of the atmospheric methane budget: what do the carbon isotopes tell us? *Atmos. Chem. Phys.* **7**, 2119–2139, doi:10.5194/acp-7-2119-2007 (2007).
12. Schwietzke, S. *et al.* Upward revision of global fossil fuel methane emissions based on isotope database. *Nature* **538**, 88–91, doi:10.1038/nature19797 (2016).
13. Mazzini, A. *et al.* Relevant methane emission to the atmosphere from a geological gas manifestation. *Scientific Reports* **11**, 4138, doi:10.1038/s41598-021-83369-9 (2021).
14. Arndt, S. *et al.* Quantifying the degradation of organic matter in marine sediments: A review and synthesis. *Earth-Science Reviews* **123**, 53–86, doi:https://doi.org/10.1016/j.earscirev.2013.02.008 (2013).
15. Dickens, G. R. Rethinking the global carbon cycle with a large, dynamic and microbially mediated gas hydrate capacitor. *Earth and Planetary Science Letters* **213**, 169–183, doi:https://doi.org/10.1016/S0012-821X(03)00325-X (2003).
16. Egger, M., Riedinger, N., Mogollón, J. M. & Jørgensen, B. B. Global diffusive fluxes of methane in marine sediments. *Nature Geoscience* **11**, 421–425, doi:10.1038/s41561-018-0122-8 (2018).
17. Piñero, E., Hensen, C., Marquardt, M., Haeckel, M. & Wallmann, K. Role of in situ organic matter degradation and fluid flow in the global gas hydrate distribution: application of general functions. *AGU Fall Meeting Abstracts -1*, 07 (2010).

18. Sowers, T. Late Quaternary Atmospheric CH₄ Isotope Record Suggests Marine Clathrates Are Stable. *Science* **311**, 838–840, doi:10.1126/science.1121235 (2006).
19. Schaefer, H. *et al.* Ice Record of δ ¹³C for Atmospheric CH₄ Across the Younger Dryas-Preboreal Transition. *Science* **313**, 1109–1112, doi:10.1126/science.1126562 (2006).
20. Etiope, G., Ciotoli, G., Schwietzke, S. & Schoell, M. Gridded maps of geological methane emissions and their isotopic signature. *Earth Syst. Sci. Data* **11**, 1–22, doi:10.5194/essd-11-1-2019 (2019).
21. Milkov, A. V. Molecular and stable isotope compositions of natural gas hydrates: A revised global dataset and basic interpretations in the context of geological settings. *Organic Geochemistry* **36**, 681–702, doi:https://doi.org/10.1016/j.orggeochem.2005.01.010 (2005).
22. Lorenson, T. D., Greinert, J. & Coffin, R. B. Dissolved methane in the Beaufort Sea and the Arctic Ocean, 1992–2009; sources and atmospheric flux. *Limnology and Oceanography* **61**, S300-S323, doi:https://doi.org/10.1002/lno.10457 (2016).
23. Berchet, A. *et al.* Atmospheric constraints on the methane emissions from the East Siberian Shelf. *Atmos. Chem. Phys.* **16**, 4147–4157, doi:10.5194/acp-16-4147-2016 (2016).
24. Berndt, C. *et al.* Temporal Constraints on Hydrate-Controlled Methane Seepage off Svalbard. *Science* **343**, 284–287, doi:doi:10.1126/science.1246298 (2014).
25. Sarkar, S. *et al.* Seismic evidence for shallow gas-escape features associated with a retreating gas hydrate zone offshore west Svalbard. *Journal of Geophysical Research: Solid Earth* **117**, doi:https://doi.org/10.1029/2011JB009126 (2012).
26. Gautier, D. L. *et al.* Assessment of Undiscovered Oil and Gas in the Arctic. *Science* **324**, 1175–1179, doi:10.1126/science.1169467 (2009).
27. Andreassen, K. *et al.* Massive blow-out craters formed by hydrate-controlled methane expulsion from the Arctic seafloor. *Science* **356**, 948–953, doi:10.1126/science.aal4500 (2017).
28. Grogan, P. *et al.* Structural elements and petroleum geology of the Norwegian sector of the northern Barents Sea. *Petroleum Geology of Northwest Europe; Proceedings of the 5th Conference* **5**, 247-259, doi:10.1144/0050247 (1999).
29. Knies, J. *et al.* The Plio-Pleistocene glaciation of the Barents Sea–Svalbard region: a new model based on revised chronostratigraphy. *Quaternary Science Reviews* **28**, 812–829, doi:https://doi.org/10.1016/j.quascirev.2008.12.002 (2009).
30. Lisiecki, L. E. & Raymo, M. E. A Pliocene-Pleistocene stack of 57 globally distributed benthic δ¹⁸O records. *Paleoceanography* **20** (2005).
31. Henriksen, E. *et al.* Chapter 17 Uplift and erosion of the greater Barents Sea: impact on prospectivity and petroleum systems. *Geological Society, London, Memoirs* **35**, 271–281, doi:10.1144/m35.17 (2011).
32. Weniger, P. *et al.* Origin of near-surface hydrocarbon gases bound in northern Barents Sea sediments. *Marine and Petroleum Geology* **102**, 455–476, doi:https://doi.org/10.1016/j.marpetgeo.2018.12.036 (2019).

33. Lutz, R. *et al.* Basin and petroleum systems modelling in the northern Norwegian Barents Sea. *Marine and Petroleum Geology* **130**, 105128, doi:<https://doi.org/10.1016/j.marpetgeo.2021.105128> (2021).
34. Ostanin, I., Anka, Z. & Di Primio, R. Role of Faults in Hydrocarbon Leakage in the Hammerfest Basin, SW Barents Sea: Insights from Seismic Data and Numerical Modelling. *Geosciences* **7**, 28 (2017).
35. Chand, S. *et al.* Multiple episodes of fluid flow in the SW Barents Sea (Loppa High) evidenced by gas flares, pockmarks and gas hydrate accumulation. *Earth and Planetary Science Letters* **331-332**, 305–314, doi:<https://doi.org/10.1016/j.epsl.2012.03.021> (2012).
36. Løtveit, I. F., Fjeldskaar, W. & Sydnes, M. Tilting and Flexural Stresses in Basins Due to Glaciations—An Example from the Barents Sea. *Geosciences* **9**, 474 (2019).
37. Medvedev, S., Hartz, E. H., Schmid, D. W., Zakariassen, E. & Varhaug, P. Influence of glaciations on North Sea petroleum systems. *Geological Society, London, Special Publications* **494**, SP494-2018-2183, doi:[10.1144/sp494-2018-183](https://doi.org/10.1144/sp494-2018-183) (2019).
38. Doré, A. G. & Jensen, L. N. The impact of late Cenozoic uplift and erosion on hydrocarbon exploration: offshore Norway and some other uplifted basins. *Global and Planetary Change* **12**, 415–436, doi:[https://doi.org/10.1016/0921-8181\(95\)00031-3](https://doi.org/10.1016/0921-8181(95)00031-3) (1996).
39. Leifer, I., Jeuthe, H., Gjøvsund, S. H. & Johansen, V. Engineered and Natural Marine Seep, Bubble-Driven Buoyancy Flows. *Journal of Physical Oceanography* **39**, 3071–3090, doi:[10.1175/2009JPO4135.1](https://doi.org/10.1175/2009JPO4135.1) (2009).
40. Leifer, I. & Patro, R. The bubble mechanism for methane transport from the shallow sea bed to the surface: A review and sensitivity study. *Continental Shelf Research* **22**, 2409–2428, doi:[10.1016/S0278-4343\(02\)00065-1](https://doi.org/10.1016/S0278-4343(02)00065-1) (2002).
41. Lasabuda, A. P. E. *et al.* Cenozoic uplift and erosion of the Norwegian Barents Shelf – A review. *Earth-Science Reviews* **217**, 103609, doi:<https://doi.org/10.1016/j.earscirev.2021.103609> (2021).
42. Laberg, J. S., Andreassen, K. & Vorren, T. O. Late Cenozoic erosion of the high-latitude southwestern Barents Sea shelf revisited. *GSA Bulletin* **124**, 77–88, doi:[10.1130/b30340.1](https://doi.org/10.1130/b30340.1) (2012).
43. NPD. Geological assessment of petroleum resources in eastern parts of the Barents Sea North. (2017).
44. Vis, G.-J. Geology and seepage in the NE Atlantic region. *Geological Society, London, Special Publications* **447**, 443–455, doi:[10.1144/sp447.16](https://doi.org/10.1144/sp447.16) (2017).
45. Sobolev, P. Cenozoic uplift and erosion of the Eastern Barents Sea - Constraints from offshore well data and the implication for petroleum system modeling. *Zeitschrift der Deutschen Gesellschaft für Geowissenschaften* **163**, 309–324, doi:[10.1127/1860-1804/2012/0163-0323](https://doi.org/10.1127/1860-1804/2012/0163-0323) (2012).
46. Spencer, A. M., Birkeland, Ø., Knag, G. Ø. & Fredsted, R. Petroleum systems of the Atlantic margin of northwest Europe. *Geological Society, London, Petroleum Geology Conference series* **5**, 231-246, doi:[10.1144/0050231](https://doi.org/10.1144/0050231) (1999).
47. Christiansen, F. Greenland petroleum exploration: history, breakthroughs in understanding and future challenges. *Geological Society, London, Memoirs* **35**, 647–661 (2011).

48. Medvedev, S., Hartz, E. H. & Faleide, J. I. Erosion-driven vertical motions of the circum Arctic: Comparative analysis of modern topography. *Journal of Geodynamics* **119**, 62–81, doi:<https://doi.org/10.1016/j.jog.2018.04.003> (2018).
49. Jakobsson, M. *et al.* The International Bathymetric Chart of the Arctic Ocean Version 4.0. *Scientific Data* **7**, 176, doi:[10.1038/s41597-020-0520-9](https://doi.org/10.1038/s41597-020-0520-9) (2020).
50. Lerch, B., Karlsen, D. A., Matapour, Z., Seland, R. & Backer-Owe, K. ORGANIC GEOCHEMISTRY OF BARENTS SEA PETROLEUM: THERMAL MATURITY AND ALTERATION AND MIXING PROCESSES IN OILS AND CONDENSATES. *Journal of Petroleum Geology* **39**, 125–148, doi:<https://doi.org/10.1111/jpg.12637> (2016).
51. Lasabuda, A. *et al.* Late Cenozoic Erosion Estimates for the Northern Barents Sea: Quantifying Glacial Sediment Input to the Arctic Ocean. *Geochemistry, Geophysics, Geosystems* **19**, 4876–4903, doi:<https://doi.org/10.1029/2018GC007882> (2018).
52. Riis, F., Lundschieen, B. A., Høy, T., Mørk, A. & E. Mørk, M. B. Evolution of the Triassic shelf in the northern Barents Sea region. *Polar Research* **27**, 318–338, doi:[10.3402/polar.v27i3.6198](https://doi.org/10.3402/polar.v27i3.6198) (2008).
53. Lundschieen, B. A., Høy, T. & Mørk, A.
54. Mau, S. *et al.* Widespread methane seepage along the continental margin off Svalbard - from Bjørnøya to Kongsfjorden. *Scientific Reports* **7**, 42997, doi:[10.1038/srep42997](https://doi.org/10.1038/srep42997) (2017).
55. Zitter, T. A. C. *et al.* Cold seeps along the main Marmara Fault in the Sea of Marmara (Turkey). *Deep Sea Research Part I: Oceanographic Research Papers* **55**, 552–570, doi:<https://doi.org/10.1016/j.dsr.2008.01.002> (2008).
56. Ferré, B. *et al.* Reduced methane seepage from Arctic sediments during cold bottom-water conditions. *Nature Geoscience* **13**, 144–148, doi:[10.1038/s41561-019-0515-3](https://doi.org/10.1038/s41561-019-0515-3) (2020).
57. Skarke, A., Ruppel, C., Kodis, M., Brothers, D. & Lobecker, E. Widespread methane leakage from the sea floor on the northern US Atlantic margin. *Nature Geoscience* **7**, 657–661, doi:[10.1038/ngeo2232](https://doi.org/10.1038/ngeo2232) (2014).
58. Amdal, F. A. *Cross-disciplinary investigation of gas seepage at Storbanken high and the Olga basin, The northern Barents Sea*, UiT Norges arktiske universitet, (2019).
59. Sahling, H. *et al.* Gas emissions at the continental margin west of Svalbard: mapping, sampling, and quantification. *Biogeosciences* **11**, 6029–6046, doi:[10.5194/bg-11-6029-2014](https://doi.org/10.5194/bg-11-6029-2014) (2014).
60. Graves, C. A. *et al.* Methane in shallow subsurface sediments at the landward limit of the gas hydrate stability zone offshore western Svalbard. *Geochimica et Cosmochimica Acta* **198**, 419–438, doi:<https://doi.org/10.1016/j.gca.2016.11.015> (2017).
61. Graves, C. A. *et al.* Fluxes and fate of dissolved methane released at the seafloor at the landward limit of the gas hydrate stability zone offshore western Svalbard. *Journal of Geophysical Research - Oceans* **120**, 6185–6201, doi:[10.1002/2015jc011084](https://doi.org/10.1002/2015jc011084) (2015).
62. Brendryen, J., Hafliðason, H., Yokoyama, Y., Haaga, K. A. & Hannisdal, B. Eurasian Ice Sheet collapse was a major source of Meltwater Pulse 1A 14,600 years ago. *Nature Geoscience* **13**, 363–368, doi:[10.1038/s41561-020-0567-4](https://doi.org/10.1038/s41561-020-0567-4) (2020).

63. Hornafius, J. S., Quigley, D. & Luyendyk, B. P. The world's most spectacular marine hydrocarbon seeps (Coal Oil Point, Santa Barbara Channel, California): Quantification of emissions. *Journal of Geophysical Research: Oceans* **104**, 20703–20711, doi:<https://doi.org/10.1029/1999JC900148> (1999).
64. Shakhova, N. *et al.* Ebullition and storm-induced methane release from the East Siberian Arctic Shelf. *Nature Geoscience* **7**, 64–70, doi:[10.1038/ngeo2007](https://doi.org/10.1038/ngeo2007) (2014).
65. Silyakova, A. *et al.* Physical controls of dynamics of methane venting from a shallow seep area west of Svalbard. *Continental Shelf Research* **194**, 104030, doi:<https://doi.org/10.1016/j.csr.2019.104030> (2020).
66. Gros, J., Arey, J. S., Socolofsky, S. A. & Dissanayake, A. L. Dynamics of Live Oil Droplets and Natural Gas Bubbles in Deep Water. *Environmental Science & Technology* **54**, 11865–11875, doi:[10.1021/acs.est.9b06242](https://doi.org/10.1021/acs.est.9b06242) (2020).
67. Platt, S. M. *et al.* Methane at Svalbard and over the European Arctic Ocean. *Atmos. Chem. Phys.* **18**, 17207–17224, doi:[10.5194/acp-18-17207-2018](https://doi.org/10.5194/acp-18-17207-2018) (2018).
68. Solomon, E. A., Kastner, M., MacDonald, I. R. & Leifer, I. Considerable methane fluxes to the atmosphere from hydrocarbon seeps in the Gulf of Mexico. *Nature Geoscience* **2**, 561–565, doi:[10.1038/ngeo574](https://doi.org/10.1038/ngeo574) (2009).
69. Tennyson, M. E. & Pitman, J. K. Geology and assessment of undiscovered oil and gas resources of the Sverdrup Basin Province, Arctic Canada, 2008. Report No. 2330-7102, (US Geological Survey, 2008).
70. Saqab, M. M., Childs, C., Walsh, J. & Delogkos, E. Multiphase deformation history of the Porcupine Basin, offshore west Ireland. *Basin Research* **33**, 1776–1797, doi:<https://doi.org/10.1111/bre.12535> (2021).
71. Gautier, D. L. Assessment of undiscovered oil and gas resources of the East Greenland Rift Basins Province. Report No. 2327–6932, (Geological Survey (US), 2007).
72. Christiansen, F. G., Bojesen-Koefoed, J. A., Dam, G., Laier, T. & Salehi, S. A review of oil and gas seepage in the Nuussuaq Basin, West Greenland—implications for petroleum exploration. *GEUS Bulletin* **44**, 10.34194/geusb. v34144. 34567 (2020).
73. Paull, C. K., Ussler, W., III, Borowski, W. S. & Spiess, F. N. Methane-rich plumes on the Carolina continental rise: Associations with gas hydrates. *Geology* **23**, 89–92, doi:[10.1130/0091-7613\(1995\)023<0089:Mrpotc>2.3.Co;2](https://doi.org/10.1130/0091-7613(1995)023<0089:Mrpotc>2.3.Co;2) (1995).
74. Colbo, K., Ross, T., Brown, C. & Weber, T. A review of oceanographic applications of water column data from multibeam echosounders. *Estuarine, Coastal and Shelf Science* **145**, 41–56, doi:<https://doi.org/10.1016/j.ecss.2014.04.002> (2014).
75. Urban, P., Köser, K. & Greinert, J. Processing of multibeam water column image data for automated bubble/seep detection and repeated mapping. *Limnology and Oceanography: Methods* **15**, 1–21, doi:<https://doi.org/10.1002/lom3.10138> (2017).

76. Dupré, S. *et al.* Tectonic and sedimentary controls on widespread gas emissions in the Sea of Marmara: Results from systematic, shipborne multibeam echo sounder water column imaging. *Journal of Geophysical Research: Solid Earth* **120**, 2891–2912, doi:<https://doi.org/10.1002/2014JB011617> (2015).
77. Römer, M. *et al.* Amount and Fate of Gas and Oil Discharged at 3400 m Water Depth From a Natural Seep Site in the Southern Gulf of Mexico. *Frontiers in Marine Science* **6**, doi:10.3389/fmars.2019.00700 (2019).
78. Römer, M. *et al.* Assessing marine gas emission activity and contribution to the atmospheric methane inventory: A multidisciplinary approach from the Dutch Dogger Bank seep area (North Sea). *Geochemistry, Geophysics, Geosystems* **18**, 2617–2633, doi:<https://doi.org/10.1002/2017GC006995> (2017).
79. Thorsnes, T. C., S. Gas flares in the Barents Sea, northeast of Kvitøya. (Geological Survey of Norway, 2018).
80. Krämer, K. & Winter, C. Predicted ripple dimensions in relation to the precision of in situ measurements in the southern North Sea. *Ocean Sci.* **12**, 1221–1235, doi:10.5194/os-12-1221-2016 (2016).
81. Planke, S., Berndt, C., Mienert, J. & Bünz, S. in *INVEST 2009 Workshop*. 25.

Figures

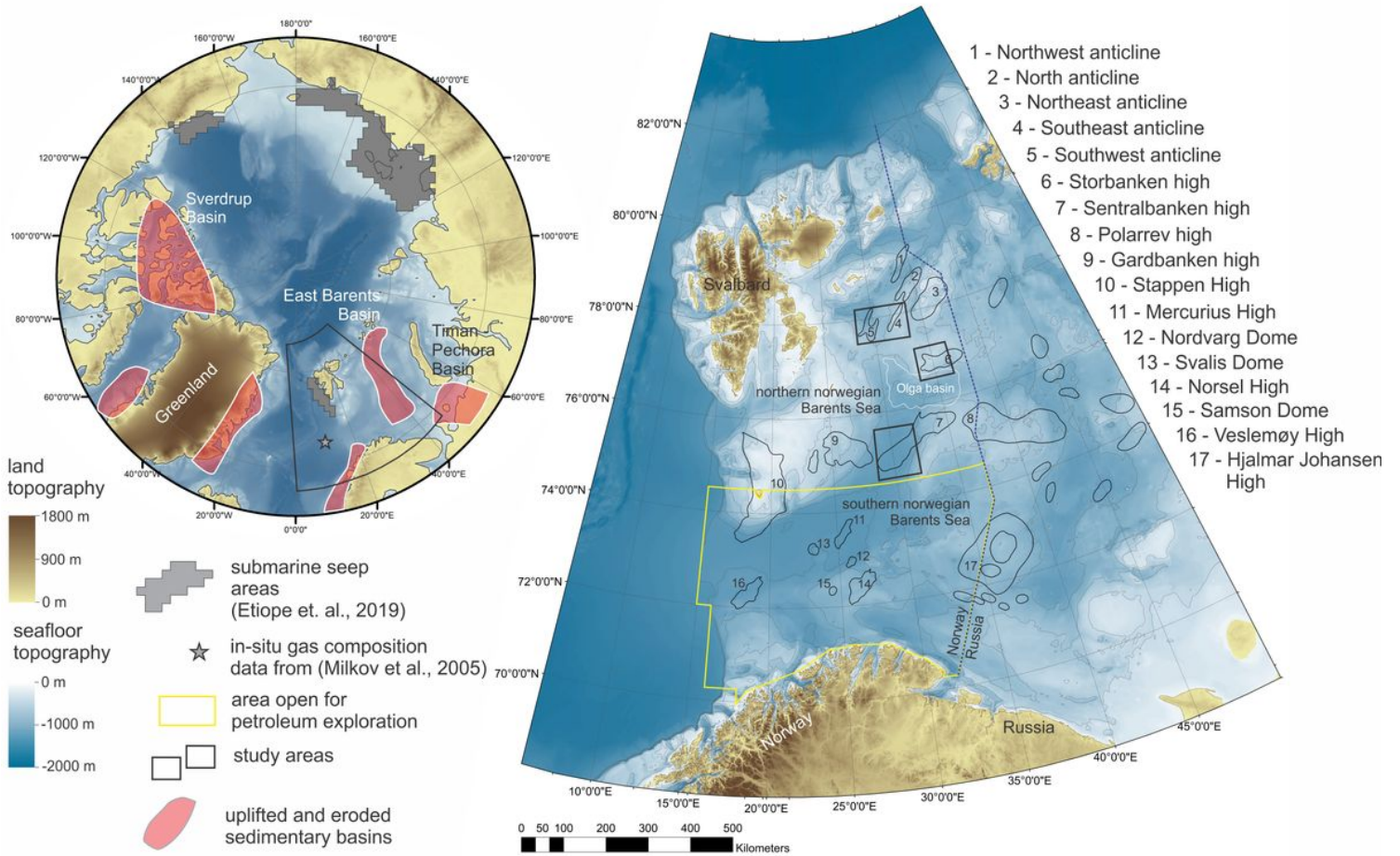


Figure 1

Structural elements⁴³ of the Barents Sea in the context of tectonically uplifted and glacially eroded Arctic sedimentary basins^{31,44-48}, with the naming conventions following Norwegian Stratigraphical Committee. Bathymetric maps are based on IBCAO V4 data⁴⁹.

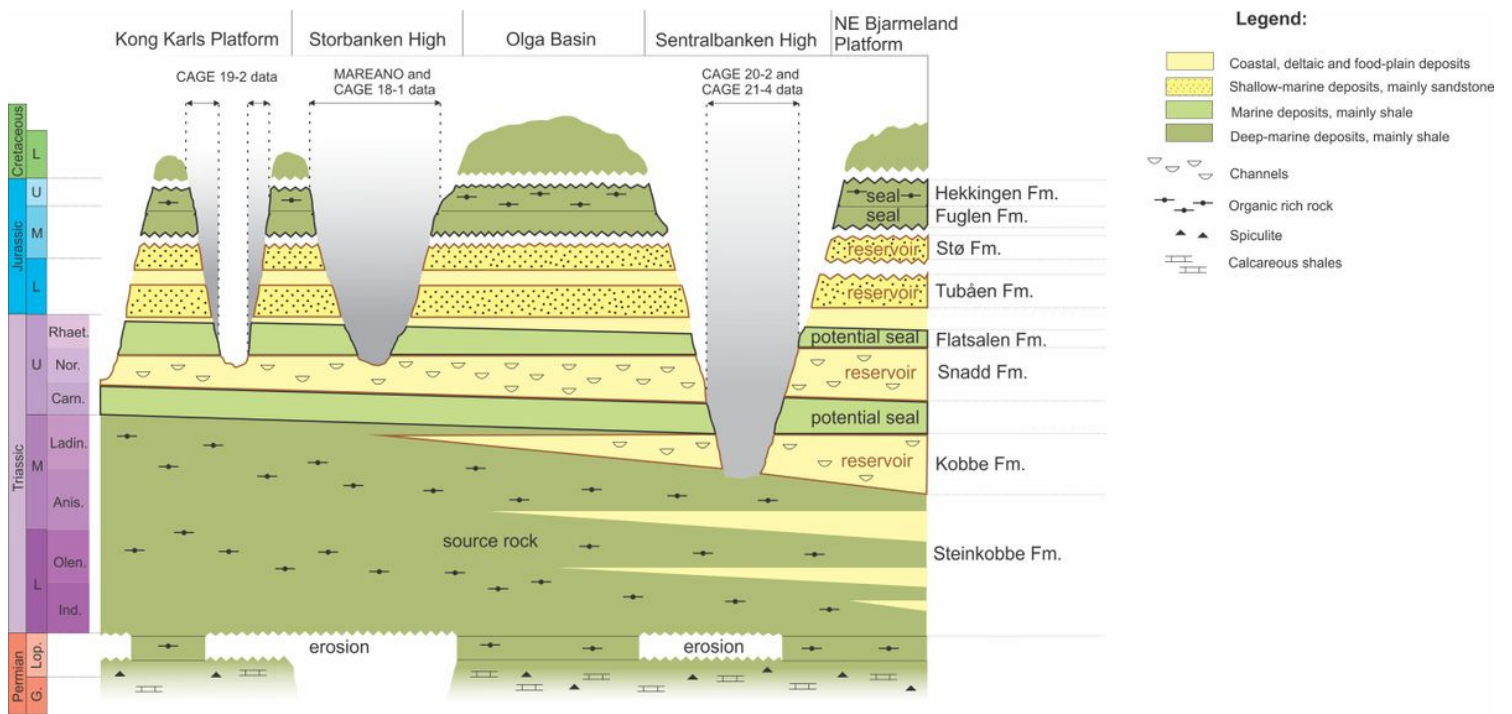


Figure 2

Lithostratigraphic diagram for the northern Norwegian Barents Sea shelf (modified from⁴³) Bold black lines outline potential reservoir formations, bold brown lines outline reservoir units. The erosional topography and thickness of the lithostratigraphic units are not to scale.

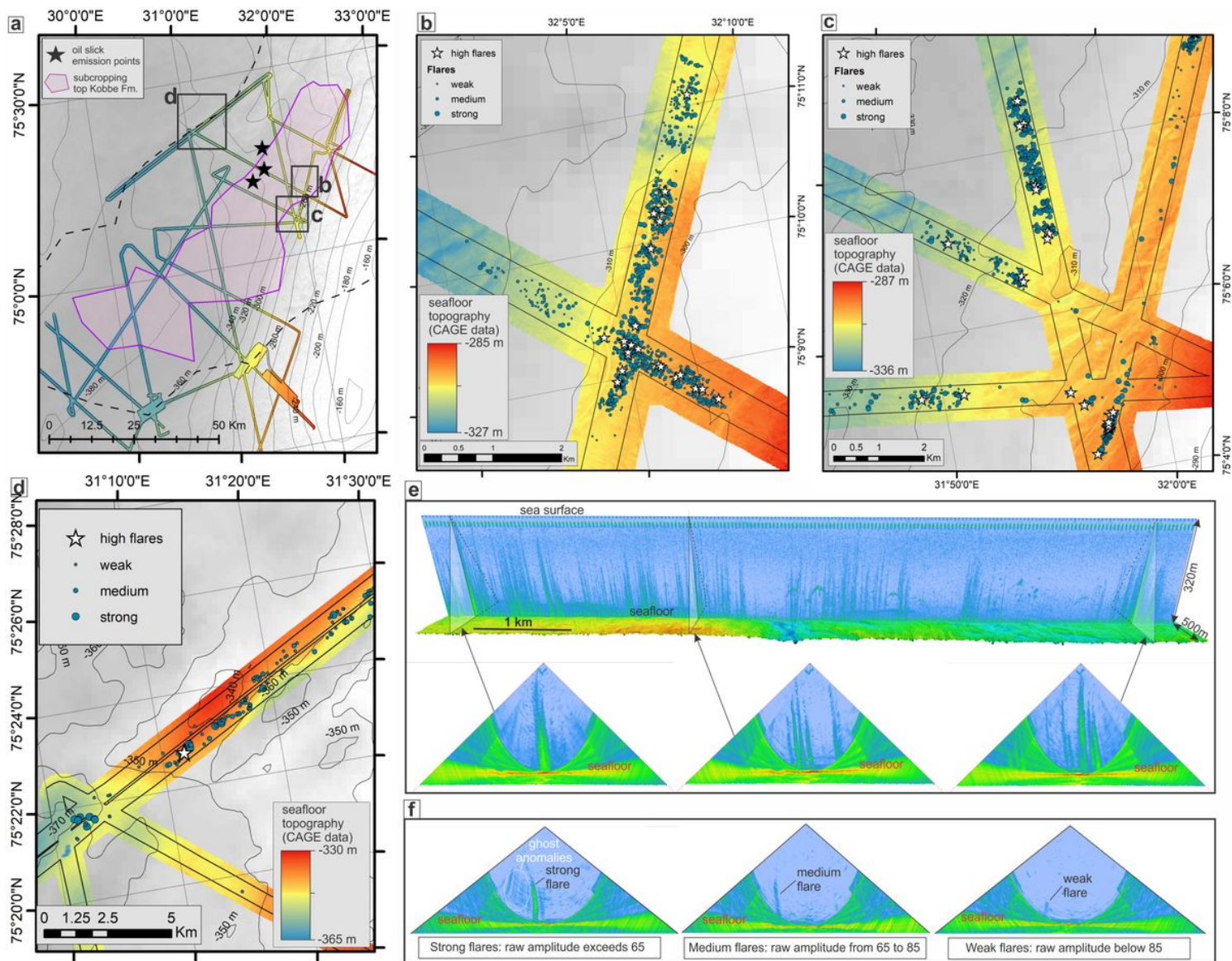


Figure 3

Imaging and mapping of the gas release at Sentralbanken high. a – d Locations of gas flares at Sentralbanken high. Multibeam bathymetric data is shown in chromatic colour scale. IBCAO V4 bathymetric data⁴⁹ is shown in monochromatic colour scale. Black lines delineate coverage of data suitable for gas flare mapping. e Gas flares on multibeam echosounder data in stack view (top) and fan view (bottom). f Examples of strong, medium and weak acoustic gas flares.

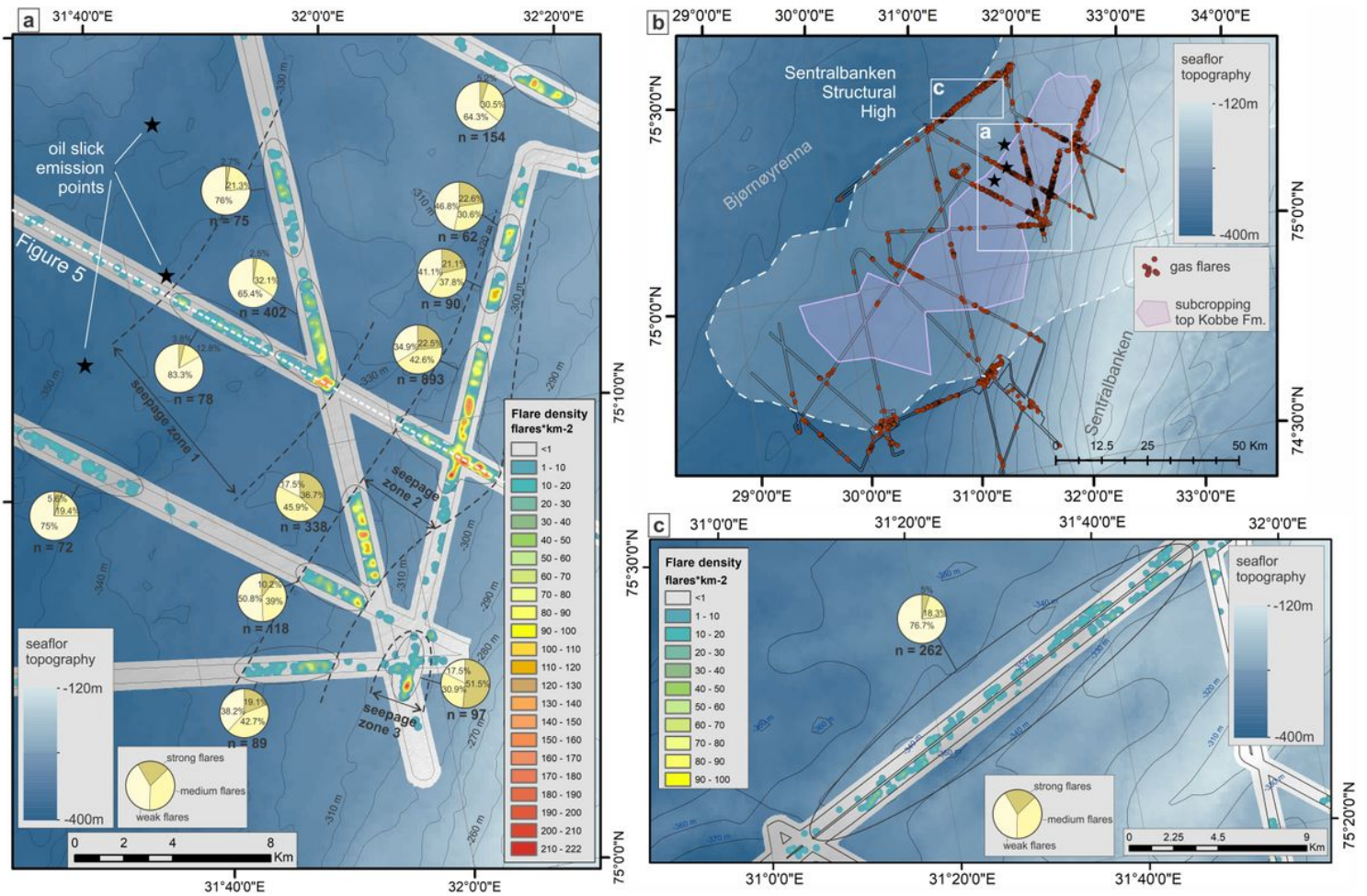


Figure 4

Density of gas flare appearance and ratios between strong, moderate and weak flares. Multibeam bathymetric data are shown in monochromatic color scale. IBCAO V4 gridded bathymetric data⁴⁹ are shown in blue color scale. a Central part of the Sentralbanken high. b Flare distribution within entire data set from Sentralbanken high. c Flare densities along the compressional fault zone.

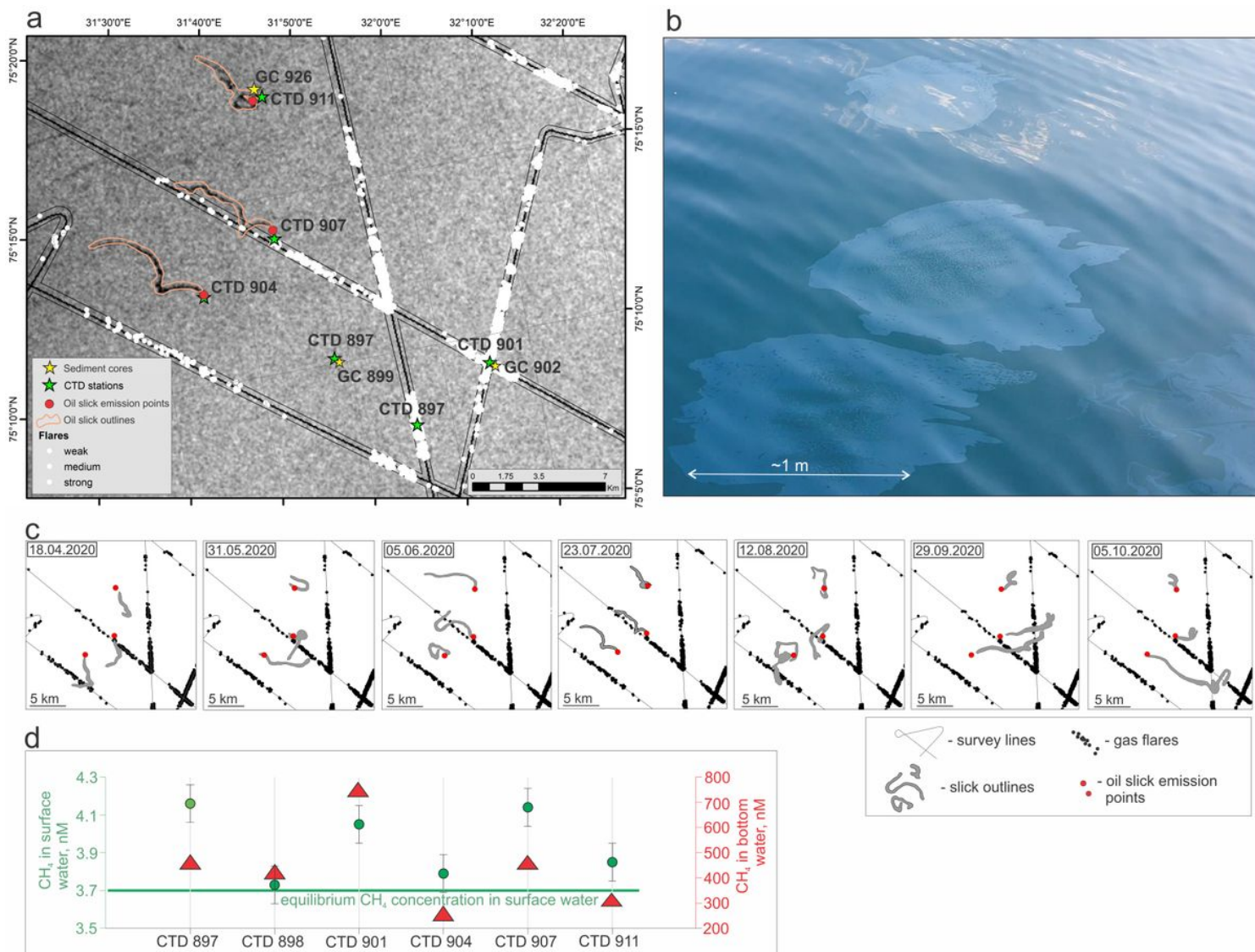


Figure 5

Indications of methane gas and oil in sea water. a Synthetic aperture radar (SAR) image s1b-ew-grd-hh-20200723t051748 of oil slicks on sea surface and locations of gas flares, water sampling stations and sediment cores. b Photograph of oil films taken during oil sampling in the vicinity of CTD 911 during CAGE 21-4 research cruise. c Compilation of monthly oil slick observations from April to October 2020; d Concentrations of methane dissolved in surface layer (green dots) and bottom layer (red triangles) of the water column.

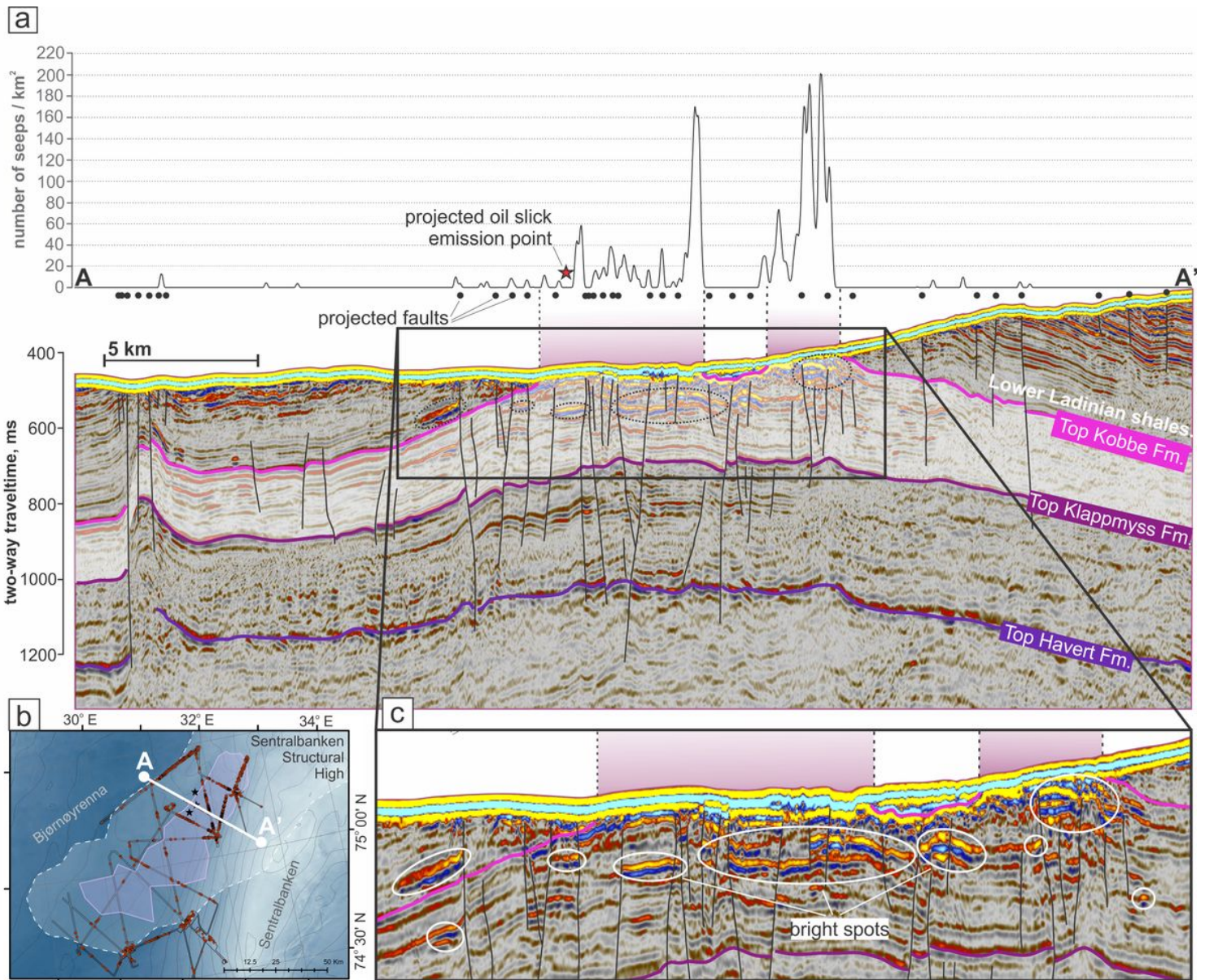


Figure 6

Correlation of gas release and subcropping reservoir Kobbe Formation and faults. a Seepage density, faults and subcropping Kobbe Formation along transect A - A'. White shading shows the reservoir. Black subvertical lines show major faults. b location of transect A - A'. c Distribution of bright spots within the apex of Sentralbanken structural high.

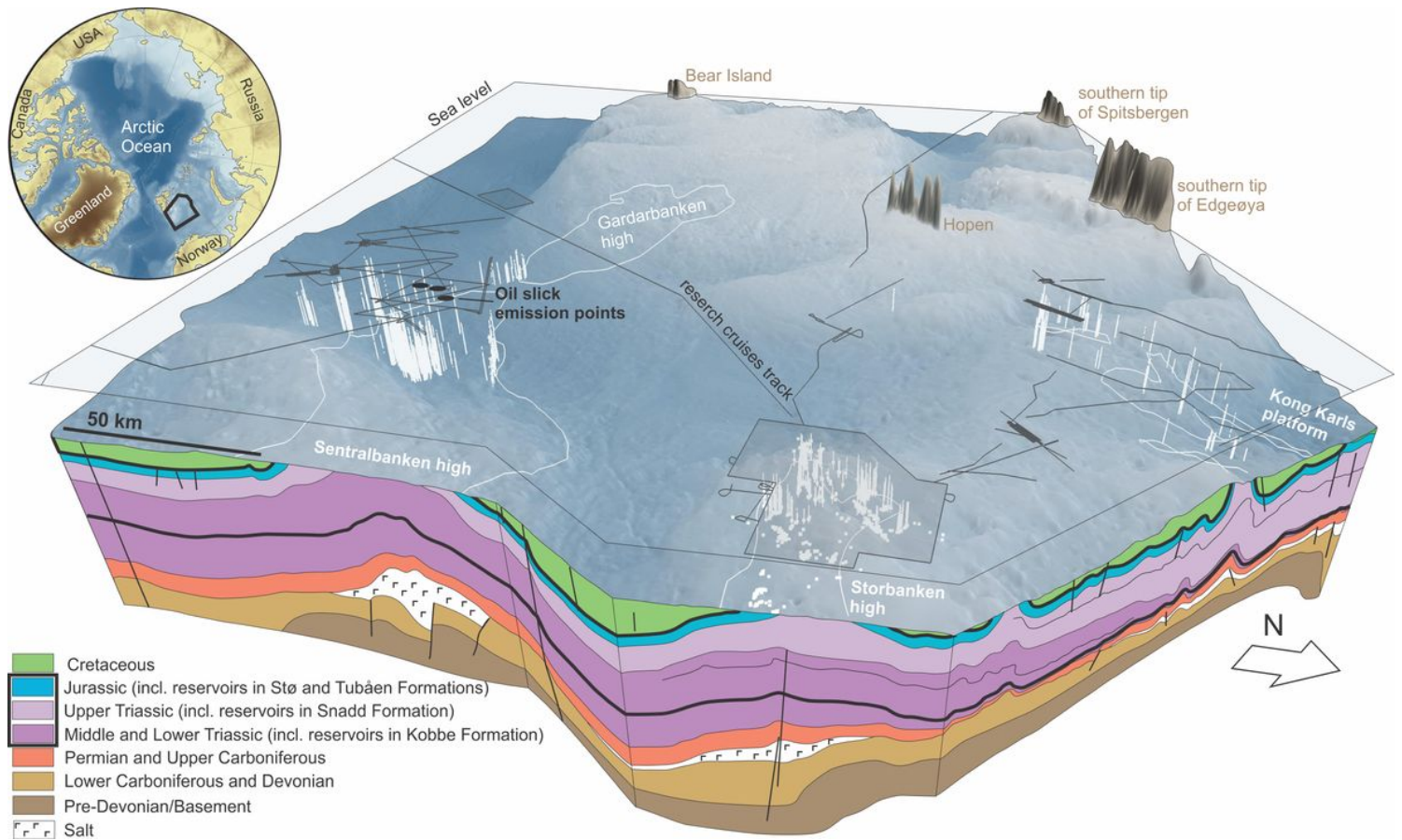


Figure 7

Exhumed hydrocarbon-bearing structures in the northern Norwegian Barents Sea emitting gas and oil to the water column. Subvertical white stripes and white dots show gas seeps. Shaded polygons on the sea surface show aerial multibeam echosounder data coverage. White polygons indicate structural boundaries. The geological profile is modified from⁴³. Bold black lines on the geological profile highlight Triassic and Jurassic hydrocarbon reservoir-bearing strata. Bathymetric data is from IBCAO V4⁴⁹.

Supplementary Files

This is a list of supplementary files associated with this preprint. Click to download.

- [Supplementary.docx](#)